



# Enhanced low-temperature performance of CO<sub>2</sub> methanation over mesoporous Ni/Al<sub>2</sub>O<sub>3</sub>-ZrO<sub>2</sub> catalysts

Jianghui Lin<sup>a</sup>, Caiping Ma<sup>b,c</sup>, Qiong Wang<sup>a</sup>, Yanfei Xu<sup>a</sup>, Guangyuan Ma<sup>a</sup>, Jie Wang<sup>a</sup>, Hongtao Wang<sup>a</sup>, Chenglong Dong<sup>a</sup>, Chenghua Zhang<sup>d</sup>, Mingyue Ding<sup>a,\*</sup>

<sup>a</sup> School of Power and Mechanical Engineering, Hubei International Scientific and Technological Cooperation Base of Sustainable Resource and Energy, Wuhan University, Wuhan 430072, China

<sup>b</sup> State Key Laboratory of Coal Conversion, Institute of Coal Chemistry, Chinese Academy of Sciences, Taiyuan 030001, China

<sup>c</sup> University of Chinese Academy of Sciences, Beijing 100049, China

<sup>d</sup> Synfuels China Co. Ltd., Beijing 101407, China

## ARTICLE INFO

### Keywords:

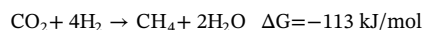
Synthetic natural gas  
CO<sub>2</sub> methanation  
Ni/Al<sub>2</sub>O<sub>3</sub>-ZrO<sub>2</sub>  
Oxygen vacancies  
Lower temperature performance

## ABSTRACT

Converting carbon dioxide to value-added chemicals has been attracted much attention, whereas direct hydrogenation of CO<sub>2</sub> to synthetic natural gas (SNG) at a lower temperature remains a big challenge. Mesoporous Al<sub>2</sub>O<sub>3</sub>-ZrO<sub>2</sub> modified Ni catalysts were prepared via a single-step epoxide-driven sol-gel method for CO<sub>2</sub> methanation. Almost 100% selectivity of CH<sub>4</sub> with 77% CO<sub>2</sub> conversion were obtained at a lower temperature of 300 °C, and no catalyst deactivation was observed in 100 h. Different characterization methods including N<sub>2</sub> adsorption-desorption, H<sub>2</sub>-TPR, H<sub>2</sub>-TPD, XRD, XPS, and TEM were combined together to explore the interaction of Ni-ZrO<sub>2</sub> and Al<sub>2</sub>O<sub>3</sub>-ZrO<sub>2</sub>. Incorporation of ZrO<sub>2</sub> into Ni/Al<sub>2</sub>O<sub>3</sub> weakened the Ni-Al<sub>2</sub>O<sub>3</sub> interaction via the combination of Al<sub>2</sub>O<sub>3</sub>-ZrO<sub>2</sub> solid solution, promoting the reduction and dispersion of NiO phase. The adding of higher Zr loading increased the amount of active metallic nickel sites and oxygen vacancies on the composite support, improving obviously the lower temperature catalytic activity and CH<sub>4</sub> selectivity. Higher Ni species loading further resulted in the formation of active Ni sites and improved the low-temperature CO<sub>2</sub> methanation performance. Moreover, the enhanced stability of the Al<sub>2</sub>O<sub>3</sub>-ZrO<sub>2</sub> support and oxygen vacancies provided by the ZrO<sub>2</sub> promoter could help to promote the catalytic stability.

## 1. Introduction

Global warming caused by greenhouse gases dominated by CO<sub>2</sub> and continuing depletion of fossil fuels have attracted considerable research attention on reducing CO<sub>2</sub> emissions and CO<sub>2</sub> utilization [1]. Many methods including CO<sub>2</sub> capture, storage and chemical conversion have been used [2], in which CO<sub>2</sub> conversion has drawn increasing interest in combination with the utilization of renewable energy resources such as solar, wind power and biomass. Conversion of CO<sub>2</sub> to hydrocarbons, methanol, synthetic natural gas (SNG) and chemicals can be realized by using H<sub>2</sub> produced with renewable energy [3–5]. Besides, limiting the fluctuation of solar and wind energy requires the storage system to stabilize the electricity grid, which highlights the advantage of SNG used as a suitable energy storage carrier [6]. The production of SNG by CO<sub>2</sub> methanation is also called Sabatier reaction, reported firstly by Paul Sabatier in 1902 [7], which is as follows:



CO<sub>2</sub> methanation is exothermic and thermodynamically favored at low temperatures, whereas kinetic limitation reduces conversion efficiency of CO<sub>2</sub> to methane [8]. The kinetics results of Yu et al. [9] indicated that the formation of bicarbonate species over the Ni-CeO<sub>2</sub> catalyst was the rate-determining step (RDS), which mainly restricted the reaction rate for CO<sub>2</sub> methanation. The results of Marocco et al. [10] suggested that formyl species formed on the surface of Ni/Al hydrotalcite-derived catalyst was supposed to be the RDS. Furthermore, potential temperature increasing during reaction and hot spot formation in the reactor result in easily the yield decline and catalyst deactivation via the sintering and carbon deposition [11]. Therefore, the designing of highly active and stable catalyst for CO<sub>2</sub> methanation at low temperature has long been pursued by researchers [12].

Transitional metals including Ni, Co, Ru, Rh and Pd have been revealed to be catalytically active for CO<sub>2</sub> methanation [13], in which noble metals (Ru, Rh, Pd) are limited to utilize in industry with large-

\* Corresponding author.

E-mail address: [dingmy@whu.edu.cn](mailto:dingmy@whu.edu.cn) (M. Ding).

<https://doi.org/10.1016/j.apcatb.2018.10.059>

Received 6 July 2018; Received in revised form 24 September 2018; Accepted 24 October 2018

Available online 26 October 2018

0926-3373/ © 2018 Elsevier B.V. All rights reserved.

scale because of their higher cost [14]. In comparison, Ni based catalysts are used widely in the CO<sub>2</sub> methanation process based on their lower price and higher catalytic activity. Wang et al. [15] investigated CO<sub>2</sub> methanation performance of Ni-based MCM-41 catalysts and obtained 85.6% CO<sub>2</sub> conversion and 99.8% CH<sub>4</sub> selectivity. The results of Rahmani et al. [16] indicated that Ni-based Al<sub>2</sub>O<sub>3</sub> catalysts presented excellent catalytic activity and superior CH<sub>4</sub> selectivity for CO<sub>2</sub> methanation. Yan et al. [17] prepared a novel NiWMgO<sub>x</sub> catalyst, which displayed 99% CH<sub>4</sub> selectivity and 83% CO<sub>2</sub> conversion at a lower reaction temperature. Recently, Vita et al. [18] manufactured a monolith-coated Ni/GDC catalyst, which improved the performance of CO<sub>2</sub> methanation. However, Ni based catalysts are easily suffered from the deactivation due to carbon deposition and nickel sintering, and hard to achieve complete conversion of CO<sub>2</sub> into CH<sub>4</sub> at low temperature [19]. The nature of supports plays an important role in affecting the dispersion of active metallic sites and metal-support interaction [20], thereby optimizing the CO<sub>2</sub> methanation performance. Extensive supports such as Al<sub>2</sub>O<sub>3</sub>, ZrO<sub>2</sub>, SiO<sub>2</sub>, TiO<sub>2</sub>, CeO<sub>2</sub> and so on have been adopted to modify Ni based catalysts [21]. Superior CO<sub>2</sub> methanation activity and CH<sub>4</sub> selectivity are displayed over CeO<sub>2</sub> [22] and/or Al<sub>2</sub>O<sub>3</sub> [23] supported Ni based catalysts by enhancing the adsorption of hydrogen and weakening the C–O bands from oxide vacancies. However, thermal sintering of active metallic Ni nanoparticles still takes place owing to their low Tammann temperature, leading to the catalyst deactivation.

Mesoporous molecular sieves (including MCM-41 and KIT-6) as potential candidates are applied to disperse Ni particles and restrain their sintering during CO<sub>2</sub> methanation [15,24]. A zeolite modified Ni catalyst prepared by Adrian et al. [25] presented 65% CO<sub>2</sub> conversion with almost 100% selectivity of CH<sub>4</sub> at 350 °C. Goodarzi et al. [26] designed a zeolite-encapsulated Ni catalyst for CO<sub>2</sub> methanation, exhibiting 60% conversion and 94% selectivity of CH<sub>4</sub> at 450 °C. However, these silica based zeolites undergo easily the mesoporous structures collapse ascribed to their hydrothermal instability. Mesoporous alumina with large surface area and good thermal stability is used as a potential support to optimize the Ni-based catalyst, which displays better CO<sub>2</sub> methanation performance at low temperature than the traditional Ni/Al<sub>2</sub>O<sub>3</sub> catalyst [27], whereas improving space still needs to be expanded for the low-temperature CO<sub>2</sub> methanation performance.

ZrO<sub>2</sub> promoter as known has excellent hydrothermal stability and higher oxygen defects to optimize the properties of support materials [12], in which the Al<sub>2</sub>O<sub>3</sub>-ZrO<sub>2</sub> composite support possessing the characteristics of high redox property, resistance to sintering and excellent thermal stability has been confirmed to be a promising support for optimizing the catalytic performance in methane reforming [28] and olefin polymerization [29]. More interestingly, the Al<sub>2</sub>O<sub>3</sub>-ZrO<sub>2</sub> composite support modified Ni catalyst has been prepared, which limits the sintering of Ni nanoparticles and carbon deposition, improving the CO methanation performance [30]. In contrast, a traditional Ni/ZrO<sub>2</sub> catalyst displays only 40% CO<sub>2</sub> conversion with about 95% selectivity of CH<sub>4</sub> at 400 °C [12]. The spatial and chemical characteristics of mesoporous Al<sub>2</sub>O<sub>3</sub>-ZrO<sub>2</sub> composite support provide us a new way to solve the obstacle in low-temperature CO<sub>2</sub> methanation, while an application of mesoporous Al<sub>2</sub>O<sub>3</sub>-ZrO<sub>2</sub> modified Ni catalysts for CO<sub>2</sub> methanation has never been reported so far.

In the present work, we prepared for the first time a Ni based catalyst supported on mesoporous Al<sub>2</sub>O<sub>3</sub>-ZrO<sub>2</sub> composite support synthesized by a single-step epoxide-driven sol-gel method, which presented a superior catalytic activity and CH<sub>4</sub> selectivity with excellent stability at a lower reaction temperature. The interaction of NiO-ZrO<sub>2</sub> and Al<sub>2</sub>O<sub>3</sub>-ZrO<sub>2</sub> was revealed detailed by characterization techniques of N<sub>2</sub> physisorption, Transmission electron microscopy (TEM), X-ray photoelectron spectroscopy (XPS), Powder X-ray diffraction (XRD), Hydrogen temperature-programmed reduction (H<sub>2</sub>-TPR) and Hydrogen temperature-programmed desorption (H<sub>2</sub>-TPD). Based on the characterization results, the structure-performance relationship was further analyzed.

## 2. Experimental

### 2.1. Catalysts preparation

A series of mesoporous Al<sub>2</sub>O<sub>3</sub>-ZrO<sub>2</sub> modified Ni catalysts with different Al/Zr molar ratios (1:0, 5:1, 2.5:1, 1:1, 1:2.5, 0:1) were synthesized by a single-step epoxide-driven sol-gel method [31,32]. Typically, a certain amount of aluminum nitrate nonahydrate and zirconium oxynitrate hydrate were dissolved in 58 ml ethanol by ultrasonic agitation, and then an appropriate amount of nickel nitrate hexahydrate were dissolved in the obtained solution with vigorous stirring. Subsequently, 29 ml 1,2-epoxypropane was added into the solution under magnetic stirring until the formation of transparent gel. After being aged for 2 days, the gel was washed with ethanol two times in order to remove the residues, and then was dried at 80 °C in a convection oven for 48 h. Finally, the resulting powder was calcined at 550 °C for 6 h. The total amounts of aluminum and zirconium precursors were 0.04 mol. The mass fraction of nickel loading was fixed at 10% for all the catalysts. The prepared mesoporous 10Ni/Al<sub>2</sub>O<sub>3</sub>-ZrO<sub>2</sub> catalysts were denoted as Ni/Al<sub>2</sub>O<sub>3</sub>-ZrO<sub>2</sub>-m (m = 5.0, 2.5, 1.0, and 0.4), where m represented the Al/Zr molar ratio. The single Ni/Al<sub>2</sub>O<sub>3</sub> and Ni/ZrO<sub>2</sub> catalysts were prepared by above method.

Mesoporous Ni/Al<sub>2</sub>O<sub>3</sub>-ZrO<sub>2</sub> catalysts with different nickel loadings were also prepared through the same process mentioned above, where the Al/Zr molar ratio was fixed at 1:1. The catalysts obtained were denoted as nNi/Al<sub>2</sub>O<sub>3</sub>-ZrO<sub>2</sub> (1, 10, 20, 30), where n represented the content of Ni in wt%.

### 2.2. Catalysts characterization

The N<sub>2</sub> adsorption-desorption analysis was carried out by an automatic physical adsorption analyzer (Micromeritics ASAP2020). The sample was degassed at 120 °C for 3 h to remove physical adsorbed water and impurities on the surface before the measurement. The specific surface area was calculated by Brunauer-Emmett-Teller (BET) method, and pore size distribution was analyzed by Barrett-Joyner-Halenda (BJH) method. Elemental analysis of as-prepared catalysts was carried out by an inductively coupled plasma optical emission spectrometer (ICP-OES).

X-ray diffraction (XRD) analysis was performed with a Bruker AXS-D8 Advance (Germany) diffractometer using Co K $\alpha$  ( $\gamma$  = 1.78 Å) radiation at 35 kV and 40 mA. XPS spectra of the catalysts were checked by a VG system (MiltiLab 2000), using an Al K $\alpha$  X-ray source (1486.6 eV). The C1 s as a reference signal was adjusted to 284.6 eV.

H<sub>2</sub>-TPR measurements were performed in a quartz tube equipped with a thermal conductivity detector (TCD). The samples were pre-treated with high purity N<sub>2</sub> at 350 °C and a flow rate of 30 mL/min for 0.5 h to remove water and other contaminants. The samples were cooled down to room temperature, and then 5% H<sub>2</sub>/N<sub>2</sub> was introduced into the system at a flow rate of 30 mL/min. The TCD signal and sample temperature were recorded while the temperature being ramped to 1000 °C at a heating rate of 10 °C/min.

H<sub>2</sub> temperature-programmed desorption (H<sub>2</sub>-TPD) experiments were carried out on a BEL-CAT B (BEL, Co., Japan). About 30 mg catalyst was charged into the quartz tube and reduced with a flow of 5% H<sub>2</sub>/Ar (30 mL/min) at 500 °C for 2 h. After that, the sample was cooled down to 30 °C, and then purged with Ar flow (30 mL/min) for 1 h to remove weakly adsorbed species. Desorption was carried out by increasing the temperature of the sample from 50 to 550 °C at 10 °C/min and held at 550 °C for 0.5 h under the flow of Ar. The moles of desorbed H<sub>2</sub> were calculated by integrating the area of the H<sub>2</sub>-TPD profiles and using calibration pulses of pure H<sub>2</sub> of known quantities. The turnover frequency (TOF) was calculated as moles of CH<sub>4</sub> produced per mole of surface metal atoms per second using the inlet flow of CO<sub>2</sub>, the molar gas volume and the catalyst mass (surface metal atoms was estimated using the dispersion from H<sub>2</sub>-TPD analysis (Fig. S1)).

Transmission electron microscopy (TEM) micrographs were obtained using a FEI Tecnai G2 F20 instrument with an acceleration voltage of 200 kV. The samples were dispersed in ethyl alcohol by ultrasonic treatment, evaporating a drop of the resultant suspension onto a carbon-coated copper grid. Carbon deposition of spent catalysts were characterized by thermodynamic analysis (TG). After drying at room temperature, a certain amount of sample was heated to 900 °C in air atmosphere with a heating rate of 10 °C/min on an Al<sub>2</sub>O<sub>3</sub> crucible.

### 2.3. CO<sub>2</sub> methanation performance

CO<sub>2</sub> methanation was performed at atmospheric pressure in a vertical continuous-flow fixed-bed reactor (inner diameter of 12 mm and a length of 330 mm). The flow of reaction gases was controlled by mass flow controllers. The actual reaction temperature of the catalyst was monitored using a thermocouple placed in the middle of the tubular reactor. 500 mg of the catalyst mixed with 500 mg quartz sand (40–70 mesh) were placed in the reactor center. Before the reaction, the catalyst was reduced in situ at 500 °C under a flow of H<sub>2</sub> at a gas hourly space velocity (GHSV) of 2000 ml·g<sup>-1</sup> h<sup>-1</sup> for 10 h, and then cooled to 160 °C. Afterwards, the mixture of H<sub>2</sub> and CO<sub>2</sub> (molar ratio H<sub>2</sub>/CO<sub>2</sub> = 4.0:1.0) was introduced into the reactor at 6000 ml·g<sup>-1</sup> h<sup>-1</sup> of GHSV. The catalytic tests were carried out at different temperatures, ranging from 160 to 460 °C.

The gas products were analyzed using an on-line gas chromatogram (Fuli 9790II) equipped with a TCD detector using porapak Q and Molecular Sieve 5A packed column. The value of CO<sub>2</sub> conversion (X<sub>CO2</sub>) and CH<sub>4</sub> selectivity (S<sub>CH4</sub>) were calculated by the following equations:

$$X_{CO_2} = \frac{W_{CO_2, in} - W_{CO_2, out}}{W_{CO_2, in}} \times 100\%$$

$$S_{CH_4} = \frac{W_{CH_4, out}}{W_{CH_4, out} + W_{CO, out}} \times 100\%$$

where W<sub>CO<sub>2</sub>, in</sub> and W<sub>CO<sub>2</sub>, out</sub> were relative volume percentage of CO<sub>2</sub> in the feed and effluent gas, and W<sub>CH<sub>4</sub>, out</sub> and W<sub>CO, out</sub> were relative volume percentage of CH<sub>4</sub> and CO in the effluent gas, respectively.

The C balances for all the tests were in the range of 92–100% (surface carbon deposition was estimated by TG. For example, the amount of carbon deposition for the spent 10Ni/Al<sub>2</sub>O<sub>3</sub>-ZrO<sub>2</sub>-1.0 catalyst was about 1% (Fig. S2)).

## 3. Results and discussion

### 3.1. Textural properties

Textural properties of the fresh Ni/Al<sub>2</sub>O<sub>3</sub>-ZrO<sub>2</sub> catalysts with different Al/Zr molar ratios were examined by nitrogen adsorption-desorption analysis, as shown in Fig. 1. The detailed textural parameters

**Table 1**  
Textural properties of the Ni/ Al<sub>2</sub>O<sub>3</sub>-ZrO<sub>2</sub> catalysts.

Sample	S <sub>BET</sub> <sup>a</sup> (m <sup>2</sup> /g)		V <sub>p</sub> <sup>b</sup> (cm <sup>3</sup> /g)		D <sub>p</sub> <sup>c</sup> (nm)		Content <sup>d</sup>	
	Fresh	Spent	Fresh	Spent	Fresh	Spent	Ni%	Al/Zr
Ni/Al <sub>2</sub> O <sub>3</sub>	291	109	0.35	0.38	3.30	9.44	7.30	—
Ni/Al <sub>2</sub> O <sub>3</sub> -ZrO <sub>2</sub> -5.0	198	121	0.21	0.19	3.18	4.14	8.11	4.51
Ni/Al <sub>2</sub> O <sub>3</sub> -ZrO <sub>2</sub> -2.5	181	102	0.21	0.15	3.65	3.80	7.91	2.23
Ni/Al <sub>2</sub> O <sub>3</sub> -ZrO <sub>2</sub> -1.0	125	74	0.14	0.12	3.34	4.43	7.90	0.88
Ni/Al <sub>2</sub> O <sub>3</sub> -ZrO <sub>2</sub> -0.4	40	11	0.04	0.01	3.13	3.55	8.22	0.38
Ni/ZrO <sub>2</sub>	2	3	0.01	0.01	5.37	6.72	7.75	—

<sup>a</sup> Calculated by the BET equation.

<sup>b</sup> BJH desorption pore volume.

<sup>c</sup> BJH desorption average pore diameter.

<sup>d</sup> Determined by ICP-OES measurement.

were listed in Table 1. It is seen from Fig. 1a that the isotherm of Ni/Al<sub>2</sub>O<sub>3</sub> displayed classic IV type curves with apparent H2 hysteresis loops (IUPAC), corresponding to the typical feature of mesoporous structure [33], indicating that the single-step epoxide-driven sol-gel method resulted in the formation of mesoporous alumina. The largest BET surface area (291 m<sup>2</sup>/g) and average pore volume (0.35 cm<sup>3</sup>/g) were presented for the mesoporous Al<sub>2</sub>O<sub>3</sub> modified Ni catalyst. In contrast, the BET surface area decreased obviously to 2 m<sup>2</sup>/g for the Ni/ZrO<sub>2</sub> catalyst, and no formation of mesoporous and/or macroporous structures was observed. As zirconium species was added into the Ni/Al<sub>2</sub>O<sub>3</sub> catalyst, the classic IV type curves with H2 hysteresis loops remained basically unchanged (Fig. 1a), indicating that incorporation of Zr species into the mesoporous Al<sub>2</sub>O<sub>3</sub> support did not changed the intrinsic morphology of Al<sub>2</sub>O<sub>3</sub>. With gradual increasing of Zr content, the area of hysteresis loops presented a decreasing trend (Fig. 1a), and average pore diameter became narrow slowly in the region of 3–4 nm (Fig. 1b), implying a decrease of the mesoporous structure volume of Al<sub>2</sub>O<sub>3</sub>-ZrO<sub>2</sub> at higher loading of Zr species. The detailed textural properties shown in Table 1 indicated that the BET surface area and average pore volume decreased obviously from 291 m<sup>2</sup>/g and 0.35 cm<sup>3</sup>/g of Ni/Al<sub>2</sub>O<sub>3</sub> to 40 m<sup>2</sup>/g and 0.04 cm<sup>3</sup>/g of Ni/Al<sub>2</sub>O<sub>3</sub>-ZrO<sub>2</sub>-0.4, which might be attributed to the increased density by zirconium incorporation [34]. Another possible reason is that higher surface energy for Zr<sup>4+</sup> than Al<sup>3+</sup> resulted in the sintering occurring between particles with high surface energies, which promoted the coalescence of mesopores, decreasing the BET surface area and average pore volume [35].

N<sub>2</sub> adsorption-desorption analysis of the used Ni/Al<sub>2</sub>O<sub>3</sub>-ZrO<sub>2</sub> catalysts were shown in Fig. S3, and corresponding textural properties were also summarized in Table 1. As shown in Figs. S3a and S3b, the relative pressure of hysteresis loops for the used Ni/Al<sub>2</sub>O<sub>3</sub> catalyst increased to 0.7–0.9 compared to the fresh Ni/Al<sub>2</sub>O<sub>3</sub> catalyst (0.4–0.6), and average

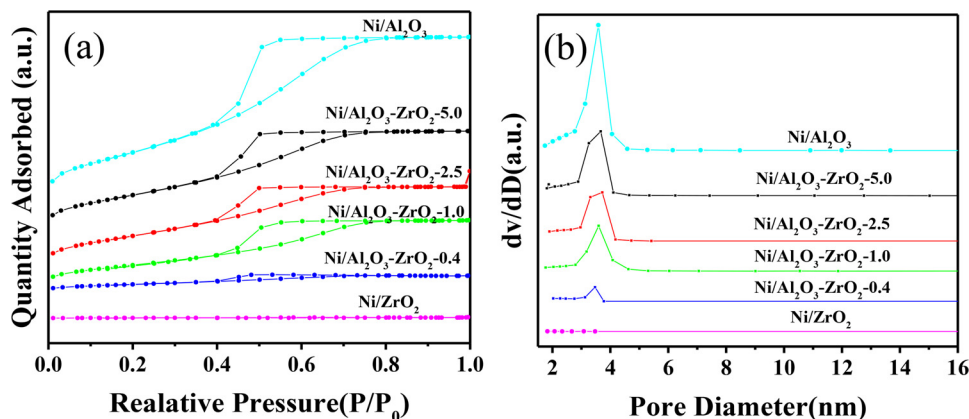


Fig. 1. (a) N<sub>2</sub> adsorption-desorption isotherms and (b) BJH pore size distributions of the fresh Ni/Al<sub>2</sub>O<sub>3</sub>-ZrO<sub>2</sub> catalysts.

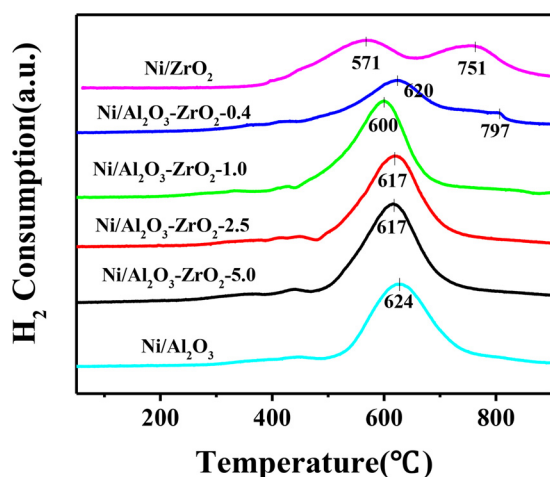


Fig. 2.  $H_2$ -TPR profiles of the fresh Ni/ $Al_2O_3$ - $ZrO_2$  catalysts.

pore size increased from 3.3 to 9.4 nm, which could be attributed to partial blockage or collapse of smaller mesopores during reaction, revealing the instability of Ni/ $Al_2O_3$  catalyst. By comparison, the classic IV type curves with  $H_2$  hysteresis loops of Ni/ $Al_2O_3$ - $ZrO_2$  catalysts were basically stable, with no obvious change of average pore size appeared during reaction (Table 1), demonstrating that incorporation of Zr species into mesoporous  $Al_2O_3$  strengthened the stability of the composite  $Al_2O_3$ - $ZrO_2$  support via the enhanced interaction between Zr and Al species [35].

### 3.2. $H_2$ -TPR analysis

The reduction behavior of Ni/ $Al_2O_3$ - $ZrO_2$  catalysts was analyzed by  $H_2$ -TPR. As shown in Fig. 2, one main reduction peak appeared at 624 °C for the Ni/ $Al_2O_3$  catalyst, which was attributed to the reduction of NiO species possessing a strong interaction with the  $Al_2O_3$  support [36,37]. Two reduction peaks shown at 570 and 750 °C for the Ni/ $ZrO_2$  catalyst corresponded to the weak and strong interaction of NiO species with  $ZrO_2$ , respectively [38]. With the increasing Zr content in the Ni/ $Al_2O_3$ - $ZrO_2$  catalysts, the reduction peak of NiO shifted slowly towards lower temperature. The reduction temperature of NiO phase decreased gradually from 624 °C of Ni/ $Al_2O_3$  to 600 °C of Ni/ $Al_2O_3$ - $ZrO_2$ -1.0, demonstrating that the adding of zirconium species into the Ni/ $Al_2O_3$ - $ZrO_2$  catalysts weakened the interaction of NiO- $Al_2O_3$  via the formation of  $Al_2O_3$ - $ZrO_2$  composite support, promoting the reduction of NiO [32]. A similar changing trend was observed by Guo et al. [30], illustrating that incorporation of  $ZrO_2$  into  $Al_2O_3$  facilitated the reduction of NiO species via weakening the NiO- $Al_2O_3$  interaction. The poor reducibility of NiO on mesoporous  $Al_2O_3$  resulted easily in insufficient active Ni sites compared to the  $Al_2O_3$ - $ZrO_2$  composite support modified Ni catalysts. An optimized reduction of NiO was obtained as the Al/Zr molar ratio decreased to 1.0 in the catalysts used in this work. Further decreasing of the Al/Zr molar ratio resulted in a slight increase in the NiO reduction temperature, which could be attributed to the addition of excessive zirconium into the Ni/ $Al_2O_3$ - $ZrO_2$  catalysts, covering abundantly on the surface of NiO and  $Al_2O_3$  support and increasing the reduction difficulty of NiO species [39].

### 3.3. XRD characterization

Fig. 3 showed X-ray diffraction profiles of Ni/ $Al_2O_3$ - $ZrO_2$  catalysts with different Al/Zr molar ratios. For the Ni/ $Al_2O_3$  catalyst, there was a weak broad peak covering the  $2\theta$  in the range of 30 to 46°, which was assigned to amorphous structure of  $Al_2O_3$ . The diffraction peaks of Ni/ $ZrO_2$  occurred at  $2\theta$  of 35.6°, 41.1°, 59.6°, 71.3° and 74.9° demonstrated the formation of  $ZrO_2$  species, composed by a mixture of orthorhombic

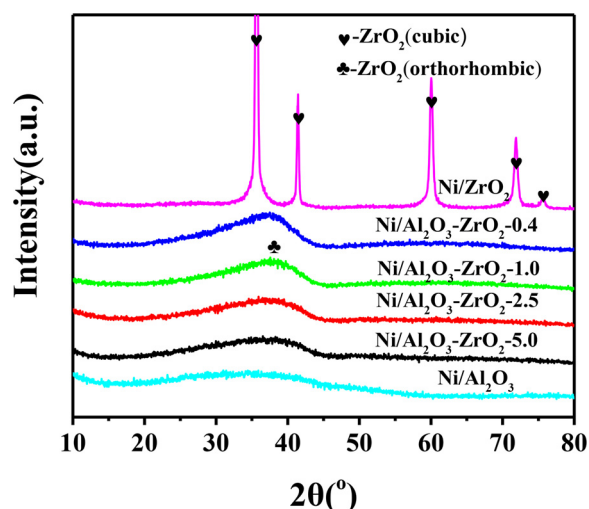


Fig. 3. XRD patterns of the fresh Ni/ $Al_2O_3$ - $ZrO_2$  catalysts.

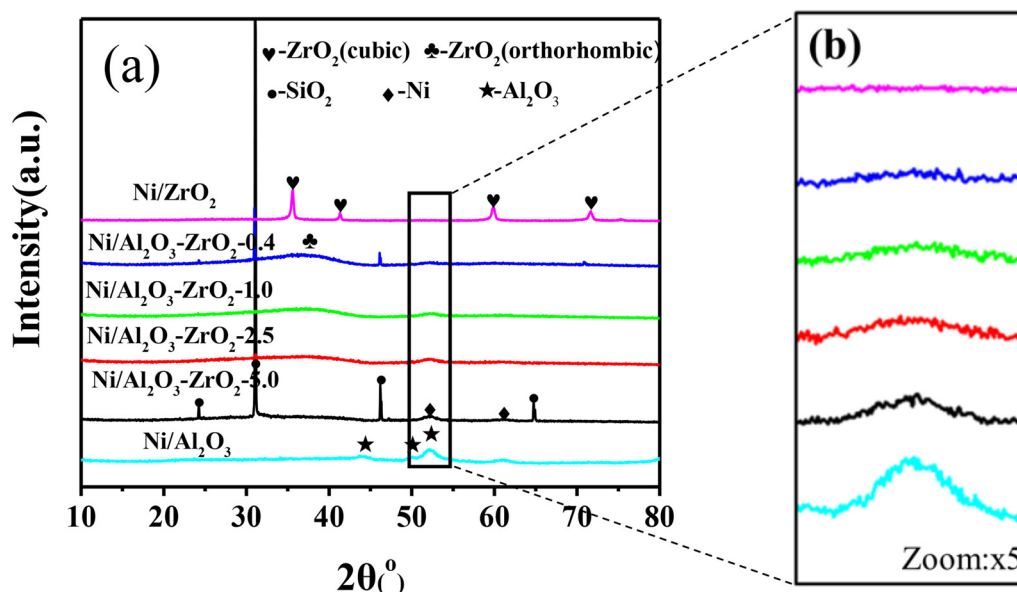
and cubic phases. The orthorhombic phase was presented at  $2\theta$  of 35.6°, while the cubic phase was presented at 41.1°, 59.6°, 71.3° and 74.9°. As zirconium species was added into the  $Al_2O_3$  support, the broad peak was narrowed slowly, and its intensity presented an increasing trend with the increasing Zr content, implying the increase of crystallization degree at higher Zr loading [35]. The shifting of broad peak towards slightly lower angle along with the increasing zirconium content might be attributed to the formation of  $Al_2O_3$ - $ZrO_2$  solid solution with Zr atoms dissolved into Al lattices [40], causing the lattice expansion of  $Al_2O_3$  because the radius of  $Zr^{4+}$  ion (0.84 Å) was larger than that of  $Al^{3+}$  ion (0.54 Å) [41]. This is in agreement with the results of Dominguez et al. [35], which displayed the formation of  $Al_2O_3$ - $ZrO_2$  solid solution with poorly crystallized phase as indicated by the broad XRD diffraction peak. In addition, no diffraction peaks of NiO were observed for the Ni/ $Al_2O_3$ - $ZrO_2$  catalysts, revealing well dispersion of NiO species on the surface of the mesoporous  $Al_2O_3$ - $ZrO_2$  support. It is possible that NiO species were small sufficiently in radius, which entered easily into the  $ZrO_2$  lattices, leading to the production of NiO- $ZrO_2$  solid solution [30]. Solid solutions such as  $ZrO_2$ - $TiO_2$  and  $ZrO_2$ - $MgO$  have been exhibited in the catalytic processes [42,43]. Combined with the  $H_2$ -TPR results mentioned above, it is proposed that introducing  $ZrO_2$  into Ni/ $Al_2O_3$  catalysts weakened the NiO- $Al_2O_3$  interaction by suppressing the entering of NiO species into the bulk regions, which played a crucial role in promoting the reduction and dispersion of NiO species [44].

The XRD patterns of the spent Ni/ $Al_2O_3$ - $ZrO_2$  catalysts were showed in Fig. 4. It is apparent from Fig. 4a that the structure of  $Al_2O_3$  and/or  $ZrO_2$  support did not changed obviously during reaction for all the catalysts. New diffraction peaks appeared at  $2\theta = 52.0^\circ$ ,  $60.7^\circ$  for the spent Ni/ $Al_2O_3$ - $ZrO_2$  catalysts, which were assigned to Ni phase (JCPDS No.01-1258). The peak intensity of metallic Ni decreased gradually with the increase of Zr content (Fig. 4b), suggesting that the adding of zirconium species into the  $Al_2O_3$  support facilitated the dispersion of Ni species on the surface layers. The results of Liu et al. [39] indicated that  $ZrO_2$  modified Ni/ $Al_2O_3$  restrained the sintering of Ni nanoparticles and decreased the Ni particles size compared to the Ni/ $Al_2O_3$  catalyst. Therefore, the adding of more Zr species into the Ni/ $Al_2O_3$ - $ZrO_2$  catalysts strengthened the anti-sintering property and promoted the dispersion of Ni nanoparticles.

### 3.4. XPS characterization

The surface phase structures of fresh and spent Ni/ $Al_2O_3$ - $ZrO_2$  catalysts were further characterized by XPS. The Al/Zr ratios calculated from XPS for as-prepared catalysts were shown in Table 2. It is seen that the Al/Zr ratio on the surface layers was higher than that in the bulk



Fig. 4. XRD patterns of the spent Ni/Al<sub>2</sub>O<sub>3</sub>-ZrO<sub>2</sub> catalysts.

**Table 2**  
Summary of XPS data for the Ni/Al<sub>2</sub>O<sub>3</sub>-ZrO<sub>2</sub> catalysts.

Sample	Ni/ZrO <sub>2</sub>	Ni/Al <sub>2</sub> O <sub>3</sub> -ZrO <sub>2</sub> -m				Ni/Al <sub>2</sub> O <sub>3</sub>
		0.4	1.0	2.5	5.0	
Zr <sup>3+</sup> /Zr <sub>T</sub> (%)	25.9	27.3	32.0	29.0	29.1	–
O <sub>A</sub> /O <sub>T</sub> (%)	62.2	68.0	73.7	71.7	72.2	61.5
Al/Zr	–	0.7	1.3	2.9	5.0	–
Ni Content (at.%)	2.7	1.1	1.4	1.5	1.0	1.1

regions obtained by ICP (Table 1), indicating that Zr species had been migrated into the bulk regions to form the Al<sub>2</sub>O<sub>3</sub>-ZrO<sub>2</sub> solid solution. This is well consistent with the XRD results. The XPS spectra in the Zr 3d region were displayed in Fig. 5. As shown in Fig. 5a, a main peak of Zr 3d<sub>5/2</sub> at 182.37 eV with a shoulder peak of Zr 3d<sub>3/2</sub> at 184.73 eV were appeared for the Ni/Al<sub>2</sub>O<sub>3</sub>-ZrO<sub>2</sub>-5.0 catalyst, corresponding to the Zr<sup>4+</sup> species [45]. The peak of Zr<sup>4+</sup> species presented an increasing trend in the intensity with the increasing Zr content, and shifted gradually towards lower binding energy (BE). The decrease of 0.3 eV BE was observed as the Al<sub>2</sub>O<sub>3</sub> support was completely replaced by ZrO<sub>2</sub>, revealing the formation of oxygen vacancies caused by ZrO<sub>2</sub> [46]. Furthermore, the fitted peak was appeared at 182.9–183.2 eV by deconvolution for all the Ni/Al<sub>2</sub>O<sub>3</sub>-ZrO<sub>2</sub> catalysts, which was attributed to the Zr<sup>3+</sup> species [47], further confirming the oxygen vacancies produced via the addition of ZrO<sub>2</sub>. Accompanied with the gradual increase of ZrO<sub>2</sub> concentration, the intensity of Zr<sup>3+</sup> species presented an increasing trend, suggesting that the amount of oxygen vacancies in the Ni/Al<sub>2</sub>O<sub>3</sub>-ZrO<sub>2</sub> catalysts could be improved by adding more ZrO<sub>2</sub> into the composite support.

After reaction, the changing trend of BE for the Zr species over the spent catalysts was similar with the fresh catalysts (Fig. 6b), implying that oxygen vacancies formed in the Ni/Al<sub>2</sub>O<sub>3</sub>-ZrO<sub>2</sub> catalysts remained stable with reaction time on stream. This is consistent with the observed results of Li et al. [47]. The ratio of Zr<sup>3+</sup> to Zr<sub>T</sub> (Zr<sub>T</sub> = Zr<sup>3+</sup> + Zr<sup>4+</sup>) calculated based on the area integrals shown in Table 2 increased firstly with the adding of Zr species, and then began to decrease as excessive Zr species was added into the Ni/Al<sub>2</sub>O<sub>3</sub>-ZrO<sub>2</sub> catalyst. An optimized Zr<sup>3+</sup>/Zr<sub>T</sub> ratio (32.0%) was obtained as the Al/Zr ratio was 1.0, demonstrating that the Ni/Al<sub>2</sub>O<sub>3</sub>-ZrO<sub>2</sub>-1.0 catalyst presented the most amount of oxygen vacancies. It is accepted that the oxygen vacancies formed on the composite Al<sub>2</sub>O<sub>3</sub>-ZrO<sub>2</sub> support play a crucial role in

adsorbing and converting CO<sub>2</sub> molecules [48].

The XPS spectra in the O 1s region for the fresh and spent catalysts were presented in Fig. 5c and d, respectively. The photoelectron peak with BE at around 530 eV was ascribed to the surface lattice oxygen (O<sub>L</sub>) of ZrO<sub>2</sub> or Al<sub>2</sub>O<sub>3</sub>, whereas the second photoelectron at 531 eV was attributed to surface adsorbed oxygen (O<sub>A</sub>) [49]. Based on the area integrals of O<sub>L</sub> and O<sub>A</sub>, the ratio of O<sub>A</sub> to O<sub>T</sub> (O<sub>T</sub> = O<sub>L</sub> + O<sub>A</sub>) for all the spent samples was summarized in Table 2. From Fig. 5c it can be seen that the O<sub>L</sub> and O<sub>A</sub> peaks of fresh Ni/ZrO<sub>2</sub> were displayed at 529.7 and 531.0 eV, while that of fresh Ni/Al<sub>2</sub>O<sub>3</sub> were located at higher BE of 530.9 and 531.9 eV, respectively. Both the O<sub>L</sub> and O<sub>A</sub> peaks were existed in the region of 529.7–530.9 eV and 531.0–531.9 eV for the Al<sub>2</sub>O<sub>3</sub>-ZrO<sub>2</sub> composite support modified Ni catalysts, respectively, and shifted gradually towards lower binding energy with the increasing Zr concentration, which might be attributed to the increasing number of oxygen vacancies in the composite Al<sub>2</sub>O<sub>3</sub>-ZrO<sub>2</sub> support with higher ZrO<sub>2</sub> concentration [47]. After reaction, the binding energy of the O<sub>L</sub> and O<sub>A</sub> peaks still shifted towards lower value with the increasing Zr content for the spent Ni/Al<sub>2</sub>O<sub>3</sub>-ZrO<sub>2</sub> catalysts (Fig. 5d), which matched with the fresh catalysts. More interestingly, the BE value of O<sub>L</sub> and O<sub>A</sub> peaks for Ni/ZrO<sub>2</sub> and Ni/Al<sub>2</sub>O<sub>3</sub> remained unchanged during reaction, whereas that for the Ni/Al<sub>2</sub>O<sub>3</sub>-ZrO<sub>2</sub> catalysts changed obviously (about 0.4 eV shifting), suggesting that the oxygen vacancies might be tuned by adjusting the Zr species amount in the Ni/Al<sub>2</sub>O<sub>3</sub>-ZrO<sub>2</sub> catalysts. The O<sub>A</sub>/O<sub>T</sub> ratio shown in Table 2 increased more obviously for the spent Ni/Al<sub>2</sub>O<sub>3</sub>-ZrO<sub>2</sub> catalyst with higher Zr/Al molar ratio than that with lower zirconium content, which was well consistent with the observation from the Zr 3d photoelectron spectra and further confirmed excellent oxygen vacancies provided by ZrO<sub>2</sub>. There existed an optimal Zr/Al molar ratio of 1.0 in terms of oxygen vacancy amounts according to analysis results of the Zr 3d and O 1s spectra.

The XPS spectra in the Ni 2p region of all the fresh and spent catalysts were shown in Fig. S4. The photoelectron peaks with BE at around 855–856 eV were ascribed to the Ni 2p<sub>3/2</sub> peaks of NiO (Fig. S4a) [50]. It can be seen that the Ni 2p<sub>3/2</sub> peak of fresh Ni/Al<sub>2</sub>O<sub>3</sub> was at 856.5 eV, which shifted gradually towards lower BE with the adding of Zr species, suggesting that the interaction of NiO-Al<sub>2</sub>O<sub>3</sub> was weakened by the adding of ZrO<sub>2</sub>, which is in accordance with the H<sub>2</sub>-TPR results. Furthermore, the intensity of NiO peak presented an increasing trend with the gradual decreasing of Al/Zr molar ratio, demonstrating that incorporation of more ZrO<sub>2</sub> into Ni/Al<sub>2</sub>O<sub>3</sub>-ZrO<sub>2</sub> catalysts promoted the formation of NiO on the surface layers via weakening the NiO-Al<sub>2</sub>O<sub>3</sub>

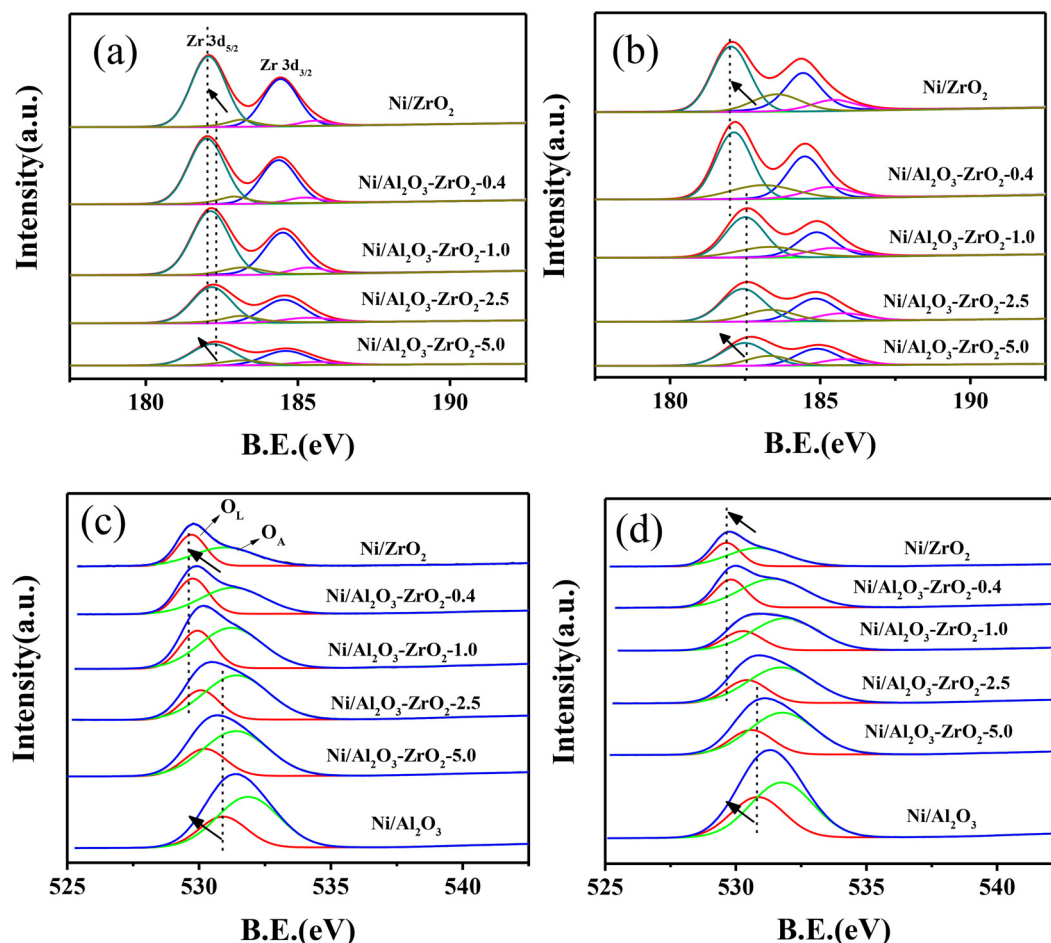


Fig. 5. XPS spectra for (a) fresh, (b) spent Ni/Al<sub>2</sub>O<sub>3</sub>-ZrO<sub>2</sub> catalysts in Zr 3d region and (c) fresh, (d) spent in O 1s region.

interaction. With continual increasing Zr concentration, the intensity of NiO peak began to decrease, which could be attributed to the partial covering of ZrO<sub>2</sub> on the surface NiO by adding excessive Zr species. After reaction, the used Ni/Al<sub>2</sub>O<sub>3</sub>-ZrO<sub>2</sub> catalysts displayed the peak of metallic Ni at around 852.3–852.6 eV (Fig. S4b). The peak intensity of metallic Ni increased gradually with the decreasing Al/Zr molar ratio, and then began to decrease as the Al/Zr molar ratio decreased to 1.0, which was consistent with the changing trend of NiO in the fresh catalysts. The amount of nickel species on the surface layers (shown in Table 2) presented an increasing trend with the decreasing Al/Zr molar ratio, further confirming that incorporation of Zr species into the Al<sub>2</sub>O<sub>3</sub> support promoted the migration of Ni species from the bulk to surface layers. As the Al/Zr molar ratio decreased to below 1.0, the amount of surface Ni species began to decrease obviously, which might be ascribed to the addition of excessive Zr species, covering on the surface of Ni species, as confirmed by H<sub>2</sub>-TPR.

### 3.5. Reaction performances

CO<sub>2</sub> methanation performances of the Ni/Al<sub>2</sub>O<sub>3</sub>-ZrO<sub>2</sub> catalysts were shown in Fig. 6. As shown in Fig. 6a, CO<sub>2</sub> conversion increased firstly for all the catalysts with increasing reaction temperature, and then began to decrease after reaching the maximum value in the specific temperature. Especially, the lowest catalytic activity and CH<sub>4</sub> selectivity as well as CH<sub>4</sub> yield were displayed at the same reaction temperature on the single Ni/ZrO<sub>2</sub> catalyst (Fig. 6a, b and c), which were consistent with the results of Perkasi et al. [51] that the traditional Ni/ZrO<sub>2</sub> catalyst resulted in the decrease of CO<sub>2</sub> methanation performance due to a lower surface area and pore size. In the present study,

the single Ni/ZrO<sub>2</sub> catalyst presented the lowest BET surface area (only 2 m<sup>2</sup>/g), which led to the fewest active sites amount formed on the catalyst, as confirmed by XPS results, decreasing obviously the CO<sub>2</sub> conversion, CH<sub>4</sub> selectivity and CH<sub>4</sub> yield. Compared to the single Ni/ZrO<sub>2</sub> catalyst, the single Ni/Al<sub>2</sub>O<sub>3</sub> catalyst exhibited higher catalytic activity and CH<sub>4</sub> selectivity as well as CH<sub>4</sub> yield at a similar reaction temperature. An optimal CO<sub>2</sub> conversion of 70.7% with 98.4% CH<sub>4</sub> selectivity and 69.5% CH<sub>4</sub> yield were obtained at 420 °C for the Ni/Al<sub>2</sub>O<sub>3</sub> catalyst.

More importantly, incorporation of ZrO<sub>2</sub> into Ni/Al<sub>2</sub>O<sub>3</sub> catalysts improved obviously the low-temperature CO<sub>2</sub> methanation performance although the single ZrO<sub>2</sub> modified Ni catalyst exhibited the lowest CO<sub>2</sub> conversion and CH<sub>4</sub> selectivity. TOF is used to evaluate the catalytic activity of Ni/Al<sub>2</sub>O<sub>3</sub>-ZrO<sub>2</sub> catalysts. As shown in Fig. 6d, the TOF value of CO<sub>2</sub> conversion increased gradually with the increasing ZrO<sub>2</sub> adding in the Al<sub>2</sub>O<sub>3</sub>-ZrO<sub>2</sub> composite support modified Ni catalysts. There was almost no TOF value displayed for the Ni/ZrO<sub>2</sub> catalyst, indicating that few active sites were produced on the Ni/ZrO<sub>2</sub> catalyst for converting CO<sub>2</sub> to CH<sub>4</sub> product. The single Ni/Al<sub>2</sub>O<sub>3</sub> catalyst displayed 0.61 s<sup>-1</sup> (TOF value), which increased to 3.87 s<sup>-1</sup> as the Al/Zr ratio decreased to 1.0 (Ni/Al<sub>2</sub>O<sub>3</sub>-ZrO<sub>2</sub>-1.0), accompanied simultaneously with the decrease of optimized reaction temperature from 420 to 340 °C, demonstrating that incorporation of zirconia into Ni/Al<sub>2</sub>O<sub>3</sub> promoted obviously the low-temperature CO<sub>2</sub> methanation performance. In addition, the temperature of CO<sub>2</sub> conversion reaching to 50% is also selected generally as the index for evaluating the catalytic performance [52]. From Fig. 6a it is apparent that the CO<sub>2</sub> methanation reaction of Ni/Al<sub>2</sub>O<sub>3</sub>-ZrO<sub>2</sub>-1.0 was initiated at 160 °C, and increased rapidly to almost 50% in CO<sub>2</sub> conversion at 260 °C, while the Ni/Al<sub>2</sub>O<sub>3</sub>

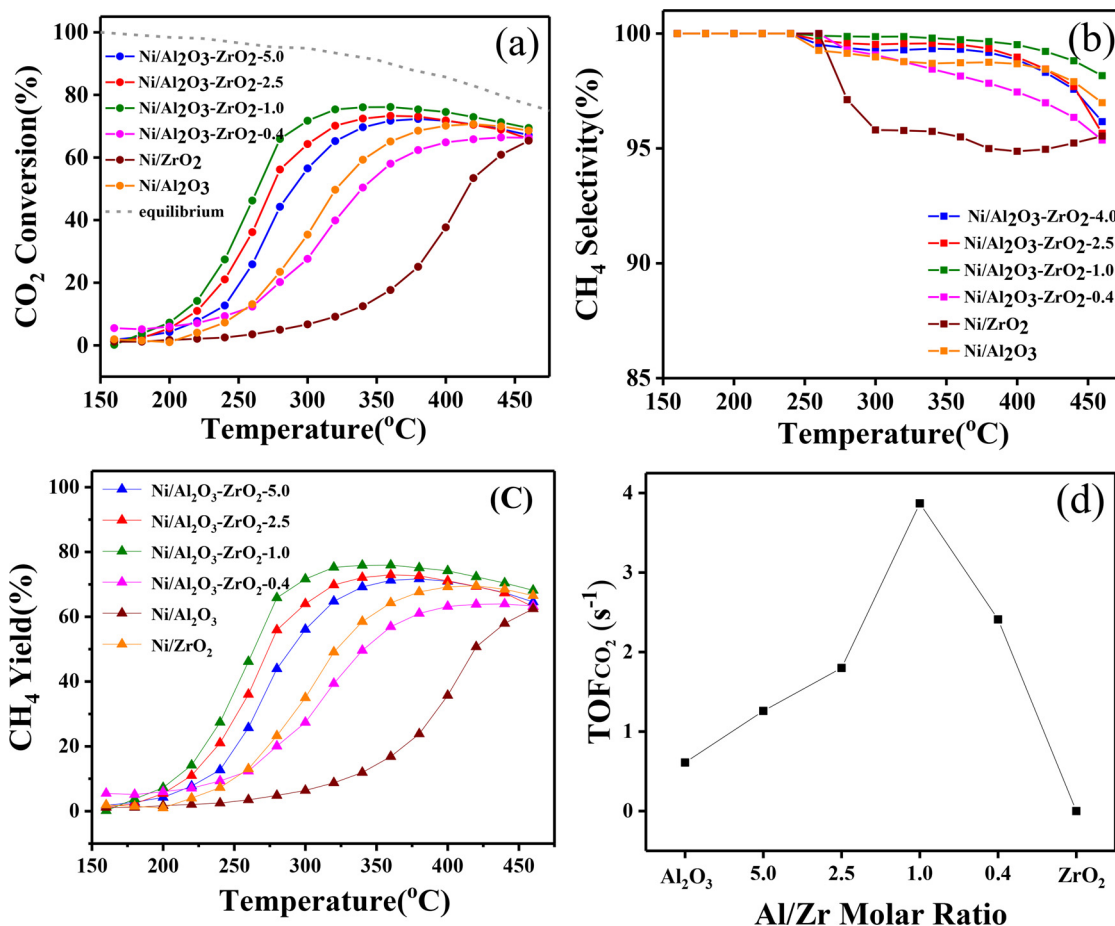


Fig. 6. (a) CO<sub>2</sub> conversion, (b) CH<sub>4</sub> selectivity, (c) CH<sub>4</sub> yield and (d) TOF values over the Ni/Al<sub>2</sub>O<sub>3</sub>-ZrO<sub>2</sub> catalysts, GHSV = 6000 ml·g<sup>-1</sup> h<sup>-1</sup>, H<sub>2</sub>/CO<sub>2</sub> = 4.

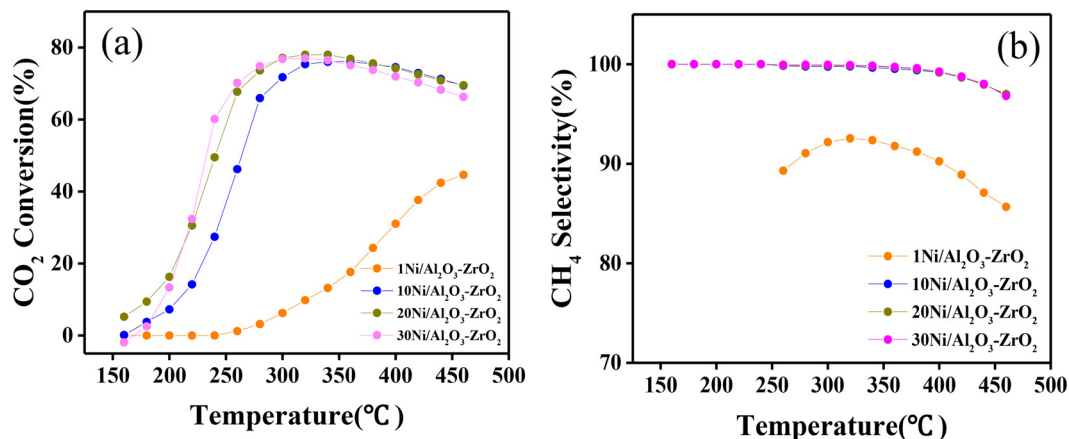


Fig. 7. (a) CO<sub>2</sub> conversion and (b) CH<sub>4</sub> selectivity over the n-Ni/Al<sub>2</sub>O<sub>3</sub>-ZrO<sub>2</sub>-1.0 catalysts, GHSV = 6000 ml·g<sup>-1</sup> h<sup>-1</sup>, H<sub>2</sub>/CO<sub>2</sub> = 4.

catalyst reached the same level in the reaction temperature higher more than 60 °C, further confirming superior low-temperature CO<sub>2</sub> methanation performance of the Ni/Al<sub>2</sub>O<sub>3</sub>-ZrO<sub>2</sub>-1.0 catalyst.

Based on the H<sub>2</sub>-TPR and XRD results mentioned above, incorporation of zirconia species suppressed the entering of NiO into the bulk region and decreased the interaction of NiO-Al<sub>2</sub>O<sub>3</sub> via the combination of ZrO<sub>2</sub>-Al<sub>2</sub>O<sub>3</sub> and ZrO<sub>2</sub>-NiO solid solutions, which promoted the reduction and dispersion of NiO species, resulting in the formation of more metallic Ni sites during pretreatment. The amount of metallic nickel sites on the surface layers presented an increasing trend with the increase of zirconia adding, as confirmed by XPS results. The maximum value of metallic nickel sites on the surface was observed as the Al/Zr

ratio decreased to 1.0. Metallic Ni species are generally considered as active sites for promoting the CO<sub>2</sub> methanation performance [11]. On the other hand, zirconia species in the Al<sub>2</sub>O<sub>3</sub>-ZrO<sub>2</sub> composite support played an important role in providing oxygen vacancies, which were expected to enhance CO<sub>2</sub> adsorption and activation [47]. The amount of oxygen vacancies increased gradually with the adding of ZrO<sub>2</sub>, and reached the maximum value over the Ni/Al<sub>2</sub>O<sub>3</sub>-ZrO<sub>2</sub>-1.0 catalyst. Therefore, the increasing amount of oxygen vacancies and active metallic Ni sites on the surface layers at higher Zr loading improved obviously the low-temperature catalytic activity and CH<sub>4</sub> selectivity. An optimized CO<sub>2</sub> conversion of 76% with almost 100% CH<sub>4</sub> selectivity at a lower reaction temperature of 340 °C were obtained for the Ni/Al<sub>2</sub>O<sub>3</sub>-

ZrO<sub>2</sub>-1.0 catalyst. As the adding of Zr loading was excessive, these Zr species would cover the surface of NiO phase, reducing the CO<sub>2</sub> methanation performance. The H<sub>2</sub>-TPR results revealed the suppressing of NiO reduction as the Al/Zr molar ratio decreased to 0.4. Synchronously, the intensity of metallic Ni on the surface layers began to decrease, as shown in XPS, which declined the amount of active metallic nickel sites for the CO<sub>2</sub> methanation reaction.

In order to further optimize the low-temperature CO<sub>2</sub> methanation performance, the Ni/Al<sub>2</sub>O<sub>3</sub>-ZrO<sub>2</sub>-1.0 catalyst with different Ni loadings were chosen and applied for the testing. As shown in Fig. 7, the lowest catalytic activity and CH<sub>4</sub> selectivity were observed for the 1Ni/Al<sub>2</sub>O<sub>3</sub>-ZrO<sub>2</sub>-1.0 catalyst, which could be attributed to the less addition of Ni species into the Ni/Al<sub>2</sub>O<sub>3</sub>-ZrO<sub>2</sub> catalyst, decreasing the amount of active Ni sites for CO<sub>2</sub> methanation. Accompanied with the increase of Ni loading, the catalytic activity increased gradually. As the Ni loading increased from 10 to 20%, the optimal reaction temperature further decreased from 340 to 300 °C, accompanied with a slight increasing of catalytic activity (77%), revealing that the increasing Ni loading on the Ni/Al<sub>2</sub>O<sub>3</sub>-ZrO<sub>2</sub> catalyst further improved the low-temperature CO<sub>2</sub> methanation performance. However, the growth momentum of CO<sub>2</sub> conversion was restrained for the 30Ni/Al<sub>2</sub>O<sub>3</sub>-ZrO<sub>2</sub>-1.0 catalyst, which presented a slight decline in the optimal catalytic activity compared to the 20Ni/Al<sub>2</sub>O<sub>3</sub>-ZrO<sub>2</sub>-1.0 catalyst, attributing probably to the aggregation of nickel nanoparticles with the adding of excessive Ni content into the Ni/Al<sub>2</sub>O<sub>3</sub>-ZrO<sub>2</sub> catalyst [16].

Fig. 8 showed the characterization results of n-Ni/Al<sub>2</sub>O<sub>3</sub>-ZrO<sub>2</sub>-1.0 catalysts. It is seen from H<sub>2</sub>-TPR (Fig. 8a) that all the n-Ni/Al<sub>2</sub>O<sub>3</sub>-ZrO<sub>2</sub>-1.0 catalysts presented one main NiO reduction peak. A weakened NiO reduction peak was appeared at about 700 °C as 1% Ni species was added. With gradual increasing of NiO content, the reduction peak

shifted towards lower temperature, and its intensity increased step by step, implying higher NiO loading in the Ni/Al<sub>2</sub>O<sub>3</sub>-ZrO<sub>2</sub> catalysts facilitated the reduction of NiO species and formation of active metallic Ni sites. However, as the amount of NiO exceeded to over 20%, the NiO reduction peak shifted slightly to higher temperature, which could be attributed to excessive adding of Ni species into the Ni/Al<sub>2</sub>O<sub>3</sub>-ZrO<sub>2</sub> catalyst, leading to the aggregation of NiO nanoparticles, thereby decreasing the reduction of NiO [16]. According to the XPS spectra in the Ni 2p region over the fresh n-Ni/Al<sub>2</sub>O<sub>3</sub>-ZrO<sub>2</sub> catalysts (Fig. 8b), a main Ni 2p<sub>3/2</sub> peak around 855.7 eV with a shoulder peak around 862.0 eV corresponding to NiO were existed on the surface layers. The intensity of NiO peaks presented an increasing trend with the gradual adding of nickel species, implying more NiO formed on the surface layers at higher Ni loading. It is proposed that more NiO phase produced on the catalyst could be converted to active metallic Ni sites, further improving the low-temperature CO<sub>2</sub> methanation performance. Especially, no apparent BE shifting of Ni 2p peaks in different Ni loadings was observed for the adding of different Ni amounts, demonstrating that incorporation of Ni species did not change the chemical environment of Ni/Al<sub>2</sub>O<sub>3</sub>-ZrO<sub>2</sub> catalysts. The bulky structures of fresh and spent n-Ni/Al<sub>2</sub>O<sub>3</sub>-ZrO<sub>2</sub> catalysts were characterized by XRD. The diffraction peaks of NiO were appeared for the fresh catalysts (Fig. 8c), and that of metallic Ni were formed for the spent catalysts (Fig. 8d). The intensity of NiO diffraction peaks showed an increasing trend with the increasing Ni content in the fresh Ni/Al<sub>2</sub>O<sub>3</sub>-ZrO<sub>2</sub> catalysts, and a similar changing trend was presented for the metallic Ni in the spent catalysts, indicating that the Ni/Al<sub>2</sub>O<sub>3</sub>-ZrO<sub>2</sub> catalyst with higher Ni loading resulted in the formation of more active metallic Ni species. This is in well agreement with the XPS results mentioned above. The NiO crystalline size of 20Ni/Al<sub>2</sub>O<sub>3</sub>-ZrO<sub>2</sub> calculated by Scherrer equation was about

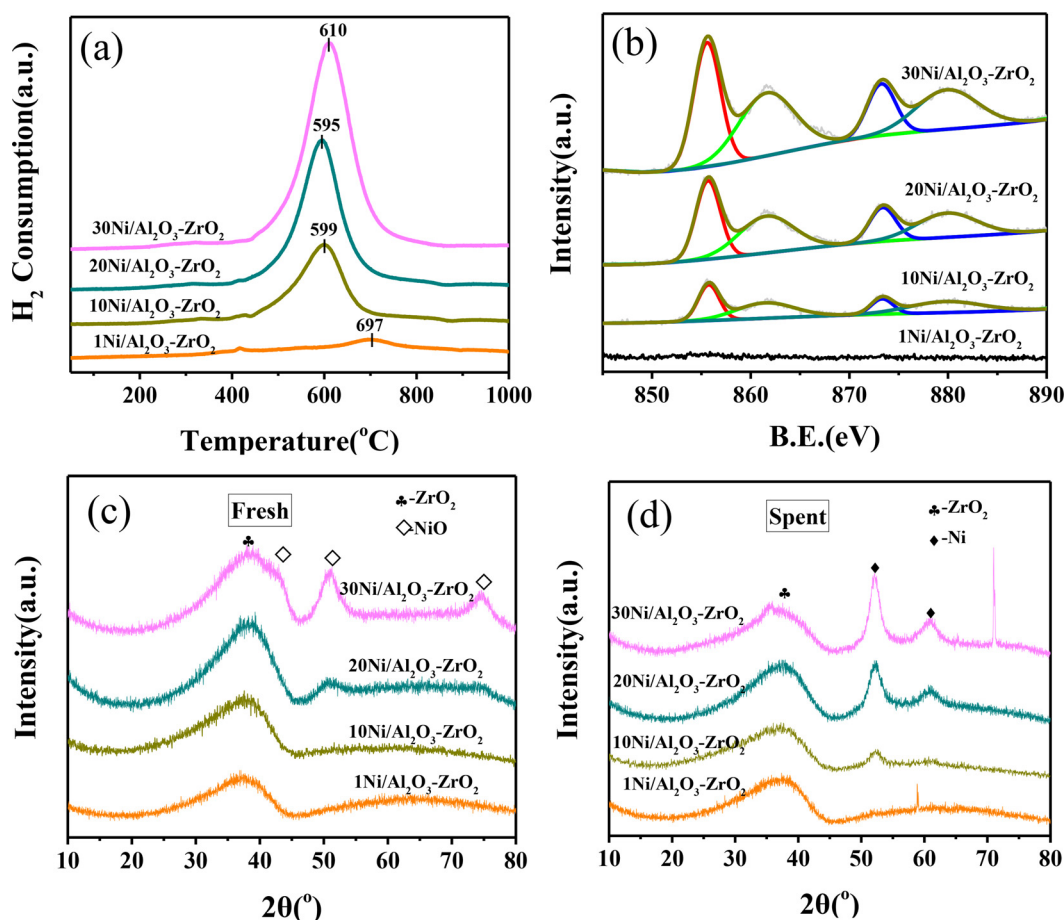


Fig. 8. (a) H<sub>2</sub>-TPR profiles (b) XPS spectra in Ni 2p region (c) fresh (d) spent XRD patterns for the n-Ni/Al<sub>2</sub>O<sub>3</sub>-ZrO<sub>2</sub>-1.0 catalysts.



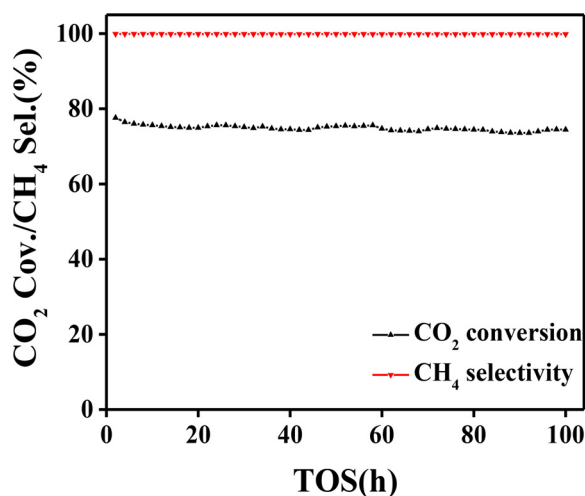


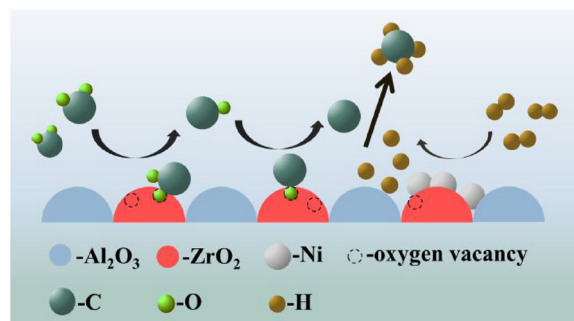
Fig. 9. Stability tests on the 20Ni/Al<sub>2</sub>O<sub>3</sub>-ZrO<sub>2</sub>-1.0 catalyst at 300 °C, GHSV = 6000 ml·g<sup>-1</sup>·h<sup>-1</sup>, H<sub>2</sub>/CO<sub>2</sub> = 4.

22 nm, which increased to 32 nm as the adding of Ni content increased to 30%. After reaction, the metallic Ni crystalline size of 30Ni/Al<sub>2</sub>O<sub>3</sub>-ZrO<sub>2</sub> increased obviously to 55 nm, suggesting that the adding of Ni species more than 20% was excessive in the study, which caused easily the aggregation of metallic Ni nanoparticles, and decreased the catalytic activity in the CO<sub>2</sub> methanation reaction.

The stability testing was carried out with 100 h on stream over the 20Ni/Al<sub>2</sub>O<sub>3</sub>-ZrO<sub>2</sub>-1.0 catalyst. As shown in Fig. 9, the 20Ni/Al<sub>2</sub>O<sub>3</sub>-ZrO<sub>2</sub>-1.0 catalyst displayed 77% of catalytic activity with almost 100% of CH<sub>4</sub> selectivity, which remained unchanged during the reaction for 100 h, demonstrating that ZrO<sub>2</sub> modified Ni/Al<sub>2</sub>O<sub>3</sub> catalysts improved dramatically the catalytic stability for CO<sub>2</sub> methanation reaction. The BET results indicated that the mesoporous Al<sub>2</sub>O<sub>3</sub> support was unstable during reaction, whereas incorporation of zirconium species strengthened the structural stabilization via forming the Al<sub>2</sub>O<sub>3</sub>-ZrO<sub>2</sub> solid solution, as confirmed by XRD technique. Another factor was the formation of oxygen vacancies on the ZrO<sub>2</sub> as certified by Zr 3d and O 1s photoelectron spectra, which could be used to active H<sub>2</sub>O produced, preventing the carbon deposition on the surface of active sites [53]. The TEM analysis of fresh and used 20Ni/Al<sub>2</sub>O<sub>3</sub>-ZrO<sub>2</sub>-1.0 catalyst was shown in Fig. S5. No obvious lattice fringes of nickel species were observed in the TEM images, implying well dispersion and low crystallinity of nickel species on the Al<sub>2</sub>O<sub>3</sub>-ZrO<sub>2</sub> composite support [54], which were in agreement with the XRD results. In addition, uniform mesopores (about 4–5 nm) could be seen for the fresh catalysts (Fig. S5a), which kept unchanged basically with time on stream during reaction (Fig. S5b), further confirming excellent stability of the Al<sub>2</sub>O<sub>3</sub>-ZrO<sub>2</sub> modified Ni catalyst.

### 3.6. Mechanism of CO<sub>2</sub> methanation

It is generally accepted that CO<sub>2</sub> adsorbed on the support combines with hydrogen atoms dissociated by active metal sites to produce CH<sub>4</sub>, although reaction pathways of CO<sub>2</sub> methanation remain ambiguous. Oxygen vacancies and/or defect sites formed on the support play a crucial role in forming surface carbon species, which react with atomic hydrogen for obtaining methane [55]. Based on the Zr 3d and O 1s XPS results, it was suggested that the ZrO<sub>2</sub> support possessed superior property of oxygen vacancies for dissociating CO<sub>2</sub> to surface carbon species, which was in consistent with the results of Li et al. [47]. Ni species is not only considered as active sites for activating CO<sub>2</sub> molecules, but also plays an important role in dissociating H<sub>2</sub> to form atomic hydrogen for Ni based catalysts in the CO<sub>2</sub> methanation reaction [56]. The ZrO<sub>2</sub> modified proposed mechanism was illustrated in Scheme 1.



Scheme 1. Proposed mechanism of CO<sub>2</sub> methanation on the Ni/Al<sub>2</sub>O<sub>3</sub>-ZrO<sub>2</sub> catalyst.

ZrO<sub>2</sub> incorporated into the Ni/Al<sub>2</sub>O<sub>3</sub> catalyst combined with Al<sub>2</sub>O<sub>3</sub> to form the composite Al<sub>2</sub>O<sub>3</sub>-ZrO<sub>2</sub> solid solution, which weakened the interaction of Ni-Al<sub>2</sub>O<sub>3</sub>, promoting the dissociation and reduction of NiO from the Al<sub>2</sub>O<sub>3</sub> support, as shown by H<sub>2</sub>-TPR. Furthermore, increasing Zr loading facilitated the dispersion of dissociated NiO and limited the aggregation of nickel nanoparticles by decreasing the free energy of surface metal species in the role of distributed ZrO<sub>2</sub> around NiO particles, providing more active metallic nickel sites for H<sub>2</sub> dissociation, as evidenced by XRD and XPS results. Besides, more oxygen vacancies provided in the higher Zr loading supplied a driving force for resolving CO<sub>2</sub> to surface carbon species, which reacted with the dissociated atomic hydrogen on the metallic Ni, promoting the product of CH<sub>4</sub> at a lower reaction temperature. More interestingly, the increasing nickel content provided the amount of more dissociated atomic hydrogen, further improving the low-temperature CO<sub>2</sub> methanation performance. As the amount of Zr loading was excessive (the Al/Zr molar ratio decreased to 0.4), the reduction of NiO was restrained and the amount of metallic Ni active sites decreased via the coverage of excessive ZrO<sub>2</sub> on the NiO surface, as revealed by H<sub>2</sub>-TPR and XPS results, which were the main reasons for the decrease of catalytic activity and CH<sub>4</sub> selectivity in the CO<sub>2</sub> methanation reaction. On the other hand, the adding of excessive nickel species resulted easily in the aggregation of Ni nanoparticles on the surface of the catalyst, decreasing the active sites for CO<sub>2</sub> methanation. This means that there existed an optimal range for both the Ni and ZrO<sub>2</sub> loadings in the effect on the low-temperature catalytic performance. Based on the results mentioned above, synergetic effect between metallic Ni active sites and ZrO<sub>2</sub>-Al<sub>2</sub>O<sub>3</sub> interaction was considered as main factors for optimizing the low-temperature CO<sub>2</sub> methanation performance. The Ni/Al<sub>2</sub>O<sub>3</sub>-ZrO<sub>2</sub> catalyst with 20 wt% Ni and 1.0 of Al/Zr molar ratio was supposed to be the most suitable catalyst in this study.

### 4. Conclusions

In summary, the mesoporous Ni/Al<sub>2</sub>O<sub>3</sub>-ZrO<sub>2</sub> catalysts with different ZrO<sub>2</sub> and Ni loadings were facilely prepared by a single-step epoxide-driven sol-gel method and applied for CO<sub>2</sub> methanation. The mesoporous Ni/Al<sub>2</sub>O<sub>3</sub>-ZrO<sub>2</sub> catalyst displayed higher catalytic activity and CH<sub>4</sub> selectivity as well as excellent stability compared to the single Ni/Al<sub>2</sub>O<sub>3</sub> and Ni/ZrO<sub>2</sub> catalysts. The characterization results indicated that incorporation of ZrO<sub>2</sub> into Ni/Al<sub>2</sub>O<sub>3</sub> weakened the interaction of Ni-Al<sub>2</sub>O<sub>3</sub> and facilitated the reduction and dispersion of NiO species. Within a certain NiO loading range, the increasing zirconia loading promoted the formation of active metallic Ni sites on the surface layers and surface oxygen vacancies, which were combined together to play a crucial role in improving the low-temperature catalytic activity and CH<sub>4</sub> selectivity. Especially, combination of ZrO<sub>2</sub> with Al<sub>2</sub>O<sub>3</sub> strengthened the interaction of Al<sub>2</sub>O<sub>3</sub>-ZrO<sub>2</sub>, facilitated the dispersion of metallic Ni nanoparticles, improving the catalytic stability in the CO<sub>2</sub> methanation reaction. An optimized CO<sub>2</sub> conversion of 77% with almost

100% CH<sub>4</sub> selectivity at a lower temperature of 300 °C were obtained for the 20Ni/Al<sub>2</sub>O<sub>3</sub>-ZrO<sub>2</sub>-1.0 catalyst, which presented excellent stability during reaction for 100 h.

## Acknowledgments

The authors gratefully acknowledge the financial support from International cooperation and exchange program of the National Natural Science Foundation of China (51861145102), International Science and Technology cooperation project of Xinjiang Production and Construction Corps (2017BC008), and Fundamental Research Fund for the Central Universities (2042017kf0173).

## Appendix A. Supplementary data

Supplementary data associated with this article can be found, in the online version, at <https://doi.org/10.1016/j.apcatb.2018.10.059>.

## References

- [1] S. Rönsch, J. Schneider, S. Matthischke, M. Schlüter, M. Götz, J. Lefebvre, P. Prabhakaran, S. Bajohr, Review on methanation - from fundamentals to current projects, *Fuel* 166 (2016) 276–296, <https://doi.org/10.1016/j.fuel.2015.10.111>.
- [2] I. Dimitriou, P. García-Gutiérrez, R.H. Elder, R.M. Cuéllar-Franca, A. Azapagic, R.W.K. Allen, Carbon dioxide utilisation for production of transport fuels: Process and economic analysis, *Energy Environ. Sci.* 8 (2015) 1775–1789, <https://doi.org/10.1039/c4ee04117h>.
- [3] K. Larmier, W.C. Liao, S. Tada, E. Lam, R. Verel, A. Bansode, A. Urakawa, A. Comas-Vives, C. Copéret, CO<sub>2</sub>-to-Methanol Hydrogenation on Zirconia-Supported Copper Nanoparticles: Reaction Intermediates and the Role of the Metal-Support Interface, *Angew. Chem. - Int. Ed.* 56 (2017) 2318–2323, <https://doi.org/10.1002/anie.201610166>.
- [4] C. Janke, M.S. Duyar, M. Hoskins, R. Farrauto, Catalytic and adsorption studies for the hydrogenation of CO<sub>2</sub> to methane, *Appl. Catal. B Environ.* 152–153 (2014) 184–191, <https://doi.org/10.1016/j.apcatb.2014.01.016>.
- [5] M.S. Duyar, M.A.A. Treviño, R.J. Farrauto, Dual function materials for CO<sub>2</sub> capture and conversion using renewable H<sub>2</sub>, *Appl. Catal. B Environ.* 168–169 (2015) 370–376, <https://doi.org/10.1016/j.apcatb.2014.12.025>.
- [6] P. Panagiotopoulou, Methanation of CO<sub>2</sub> over alkali-promoted Ru/TiO<sub>2</sub> catalysts: II. Effect of alkali additives on the reaction pathway, *Appl. Catal. B Environ.* 236 (2018) 162–170, <https://doi.org/10.1016/j.apcatb.2018.05.028>.
- [7] M. Aresta, A. Dibenedetto, Utilisation of CO<sub>2</sub> as a chemical feedstock: opportunities and challenges, *Dalton Trans.* 28 (2007) 2975–2992, <https://doi.org/10.1039/b700658f>.
- [8] A. Beuls, C. Swalus, M. Jacquemin, G. Heyen, A. Karelavic, P. Ruiz, Methanation of CO<sub>2</sub>: further insight into the mechanism over Rh/γ-Al<sub>2</sub>O<sub>3</sub> catalyst, *Appl. Catal. B Environ.* 113–114 (2012) 2–10, <https://doi.org/10.1016/j.apcatb.2011.02.033>.
- [9] Y. Yu, Y.M. Chan, Z. Bian, F. Song, J. Wang, Q. Zhong, S. Kawi, Enhanced performance and selectivity of CO<sub>2</sub> methanation over g-C<sub>3</sub>N<sub>4</sub> assisted synthesis of Ni-CeO<sub>2</sub> catalyst: kinetics and DRIFTS studies, *Int. J. Hydrogen Energy* 43 (2018) 15191–15204, <https://doi.org/10.1016/j.ijhydene.2018.06.090>.
- [10] P. Marocco, E.A. Morosanu, E. Giglio, D. Ferrero, C. Mebrahtu, A. Lanzini, S. Abate, S. Bensaid, S. Perathoner, M. Santarelli, R. Pirone, G. Centi, CO<sub>2</sub> methanation over Ni/Al hydrotalcite-derived catalyst: Experimental characterization and kinetic study, *Fuel* 225 (2018) 230–242, <https://doi.org/10.1016/j.fuel.2018.03.137>.
- [11] J. Gao, Q. Liu, F. Gu, B. Liu, Z. Zhong, F. Su, Recent advances in methanation catalysts for the production of synthetic natural gas, *RSC Adv.* 5 (2015) 22759–22776, <https://doi.org/10.1039/c4ra16114a>.
- [12] M. Romero-Sáez, A.B. Dongil, N. Benito, R. Espinoza-González, N. Escalona, F. Gracia, CO<sub>2</sub> methanation over nickel-ZrO<sub>2</sub> catalyst supported on carbon nanotubes: A comparison between two impregnation strategies, *Appl. Catal. B Environ.* 237 (2018) 817–825, <https://doi.org/10.1016/j.apcatb.2018.06.045>.
- [13] M. Younas, L. Loong Kong, M.J.K. Bashir, H. Nadeem, A. Shehzad, S. Sethupathi, Recent Advancements, Fundamental challenges, and opportunities in catalytic methanation of CO<sub>2</sub>, *Energy Fuels* 30 (2016) 8815–8831, <https://doi.org/10.1021/acs.energyfuels.6b01723>.
- [14] P. Frontera, A. Macario, M. Ferraro, P. Antonucci, Supported catalysts for CO<sub>2</sub> methanation: a review, *Catalysts* 7 (2017) 59, <https://doi.org/10.3390/catal7020059>.
- [15] X. Wang, L. Zhu, Y. Liu, S. Wang, CO<sub>2</sub> methanation on the catalyst of Ni/MCM-41 promoted with CeO<sub>2</sub>, *Sci. Total Environ.* 625 (2018) 686–695, <https://doi.org/10.1016/j.scitotenv.2017.12.308>.
- [16] S. Rahmani, M. Rezaei, F. Meshkani, Preparation of highly active nickel catalysts supported on mesoporous nanocrystalline γ-Al<sub>2</sub>O<sub>3</sub> for CO<sub>2</sub> methanation, *J. Ind. Eng. Chem.* 20 (2014) 1346–1352, <https://doi.org/10.1016/j.jiec.2013.07.017>.
- [17] Y. Yan, Y. Dai, H. He, Y. Yu, Y. Yang, A novel W-doped Ni-Mg mixed oxide catalyst for CO<sub>2</sub> methanation, *Appl. Catal. B Environ.* 196 (2016) 108–116, <https://doi.org/10.1016/j.apcatb.2016.05.016>.
- [18] A. Vita, C. Italiano, L. Pino, P. Frontera, M. Ferraro, V. Antonucci, Activity and stability of powder and monolith-coated Ni/GDC catalysts for CO<sub>2</sub> methanation, *Appl. Catal. B Environ.* 226 (2018) 384–395, <https://doi.org/10.1016/j.apcatb.2017.12.078>.
- [19] D. Wierzbicki, R. Baran, R. Dębek, M. Motak, M.E. Gálvez, T. Grzybek, P. Da Costa, P. Glatzel, Examination of the influence of La promotion on Ni state in hydrotalcite-derived catalysts under CO<sub>2</sub> methanation reaction conditions: operando X-ray absorption and emission spectroscopy investigation, *Appl. Catal. B Environ.* 232 (2018) 409–419, <https://doi.org/10.1016/j.apcatb.2018.03.089>.
- [20] W. Wang, J. Gong, Methanation of carbon dioxide: an overview, *Front. Chem. Eng. China* 5 (2011) 2–10, <https://doi.org/10.1007/s11705-010-0528-3>.
- [21] T.A. Le, M.S. Kim, S.H. Lee, T.W. Kim, E.D. Park, CO and CO<sub>2</sub> methanation over supported Ni catalysts, *Catal. Today* 293–294 (2017) 89–96, <https://doi.org/10.1016/j.cattod.2016.12.036>.
- [22] G. Zhou, H. Liu, K. Cui, H. Xie, Z. Jiao, G. Zhang, K. Xiong, X. Zheng, Methanation of carbon dioxide over Ni/CeO<sub>2</sub> catalysts: effects of support CeO<sub>2</sub> structure, *Int. J. Hydrogen Energy* 42 (2017) 16108–16117, <https://doi.org/10.1016/j.ijhydene.2017.05.154>.
- [23] F. Song, Q. Zhong, Y. Yu, M. Shi, Y. Wu, J. Hu, Y. Song, Obtaining well-dispersed Ni/Al<sub>2</sub>O<sub>3</sub> catalyst for CO<sub>2</sub> methanation with a microwave-assisted method, *Int. J. Hydrogen Energy* 42 (2017) 4174–4183, <https://doi.org/10.1016/j.ijhydene.2016.10.141>.
- [24] R. Merkache, I. Fehete, M. Maamache, M. Bernard, P. Turek, K. Al-Dalama, F. Garin, 3D ordered mesoporous Fe-KIT-6 catalysts for methylcyclopentane (MCP) conversion and carbon dioxide (CO<sub>2</sub>) hydrogenation for energy and environmental applications, *Appl. Catal. A Gen.* 504 (2015) 672–681, <https://doi.org/10.1016/j.apcata.2015.03.032>.
- [25] A. Quindimil, U. De-La-Torre, B. Pereda-Ayo, J.A. González-Marcos, J.R. González-Velasco, Ni catalysts with La as promoter supported over Y- and BETA- zeolites for CO<sub>2</sub> methanation, *Appl. Catal. B Environ.* 238 (2018) 393–403, <https://doi.org/10.1016/j.apcatb.2018.07.034>.
- [26] F. Goodarzi, L. Kang, F.R. Wang, F. Joensen, S. Kegnæs, J. Mielby, Methanation of carbon dioxide over zeolite-encapsulated nickel nanoparticles, *ChemCatChem* 10 (2018) 1566–1570, <https://doi.org/10.1002/cctc.201701946>.
- [27] L. Xu, F. Wang, M. Chen, J. Zhang, K. Yuan, L. Wang, K. Wu, G. Xu, W. Chen, CO<sub>2</sub> methanation over a Ni based ordered mesoporous catalyst for the production of synthetic natural gas, *RSC Adv.* 6 (2016) 28489–28499, <https://doi.org/10.1039/C6RA01139J>.
- [28] Y.F. Li, X.F. Dong, W.M. Lin, Effects of ZrO<sub>2</sub>-promoter on catalytic performance of CuZnAlO catalysts for production of hydrogen by steam reforming of methanol, *Int. J. Hydrogen Energy* 29 (2004) 1617–1621, <https://doi.org/10.1016/j.ijhydene.2004.03.001>.
- [29] J.R. Sohn, S.H. Kwon, D.C. Shin, Spectroscopic studies on NiO supported on ZrO<sub>2</sub> modified with MoO<sub>3</sub> for ethylene dimerization, *Appl. Catal. A Gen.* 317 (2007) 216–225, <https://doi.org/10.1016/j.apcata.2006.10.015>.
- [30] C. Guo, Y. Wu, H. Qin, J. Zhang, CO methanation over ZrO<sub>2</sub>/Al<sub>2</sub>O<sub>3</sub> supported Ni catalysts: a comprehensive study, *Fuel Process. Technol.* 124 (2014) 61–69, <https://doi.org/10.1016/j.fuproc.2014.02.017>.
- [31] S.J. Han, Y. Bang, J. Yoo, K.H. Kang, J.H. Song, J.G. Seo, I.K. Song, Hydrogen production by steam reforming of ethanol over mesoporous Ni-Al<sub>2</sub>O<sub>3</sub>-ZrO<sub>2</sub> aerogel catalyst, *Int. J. Hydrogen Energy* 38 (2013) 15119–15127, <https://doi.org/10.1016/j.ijhydene.2013.09.114>.
- [32] S.J. Han, Y. Bang, J.G. Seo, J. Yoo, I.K. Song, Hydrogen production by steam reforming of ethanol over mesoporous Ni-Al<sub>2</sub>O<sub>3</sub>-ZrO<sub>2</sub> xerogel catalysts: effect of Zr/Al molar ratio, *Int. J. Hydrogen Energy* 38 (2013) 1376–1383, <https://doi.org/10.1016/j.ijhydene.2012.11.057>.
- [33] P. Kim, Y. Kim, C. Kim, H. Kim, Y. Park, J.H. Lee, I.K. Song, J. Yi, Synthesis and characterization of mesoporous alumina as a catalyst support for hydrodechlorination of 1,2-dichloropropane: Effect of catalyst preparation method, *Catal. Lett.* 89 (2003) 185–192, <https://doi.org/10.1023/A:1025794127243>.
- [34] A.C. Faro, K.R. Souza, V.L.D.L. Camorim, M.B. Cardoso, Zirconia-alumina mixing in alumina-supported zirconia prepared by impregnation with solutions of zirconium acetylacetonate, *Phys. Chem. Chem. Phys.* 5 (2003) 1932–1940, <https://doi.org/10.1039/b300899a>.
- [35] J.M. Domínguez, J.L. Hernandez, G. Sandoval, Surface and catalytic properties of Al<sub>2</sub>O<sub>3</sub>-ZrO<sub>2</sub> solid solutions prepared by sol-gel methods, *Appl. Catal. A Gen.* 197 (2000) 119–130, [https://doi.org/10.1016/S0926-860X\(99\)00542-6](https://doi.org/10.1016/S0926-860X(99)00542-6).
- [36] A. Zhao, W. Ying, H. Zhang, H. Ma, D. Fang, Ni-Al<sub>2</sub>O<sub>3</sub> catalysts prepared by solution combustion method for syngas methanation, *Catal. Commun.* 17 (2012) 34–38, <https://doi.org/10.1016/j.catcom.2011.10.010>.
- [37] D. Hu, J. Gao, Y. Ping, L. Jia, P. Gunawan, Z. Zhong, G. Xu, F. Gu, F. Su, Enhanced investigation of CO methanation over Ni/Al<sub>2</sub>O<sub>3</sub> catalysts for synthetic natural gas production, *Ind. Eng. Chem. Res.* 51 (2012) 4875–4886, <https://doi.org/10.1021/ie300049f>.
- [38] K. Zhao, W. Wang, Z. Li, Highly efficient Ni/ZrO<sub>2</sub> catalysts prepared via combustion method for CO<sub>2</sub> methanation, *J. CO<sub>2</sub> Util.* 16 (2016) 236–244, <https://doi.org/10.1016/j.jcou.2016.07.010>.
- [39] Q. Liu, F. Gu, Z. Zhong, G. Xu, F. Su, Anti-sintering ZrO<sub>2</sub>-modified Ni/α-Al<sub>2</sub>O<sub>3</sub> catalyst for CO methanation, *RSC Adv.* 6 (2016) 20979–20986, <https://doi.org/10.1039/C5RA28057E>.
- [40] V.M.S. Muthaiah, S. Mula, Effect of zirconium on thermal stability of nanocrystalline aluminium alloy prepared by mechanical alloying, *J. Alloys. Compd.* 688 (2016) 571–580, <https://doi.org/10.1016/j.jallcom.2016.07.038>.
- [41] M.H. Youn, J.G. Seo, J.C. Jung, S. Park, I.K. Song, Hydrogen production by autothermal reforming of ethanol over nickel catalyst supported on mesoporous yttria-stabilized zirconia, *Int. J. Hydrogen Energy* 34 (2009) 5390–5397, <https://doi.org/10.1016/j.ijhydene.2009.05.051>.
- [42] V. Choque, P.R. de la Piscina, D. Molyneux, N. Homs, Ruthenium supported on new

- TiO<sub>2</sub>-ZrO<sub>2</sub> systems as catalysts for the partial oxidation of methane, *Catal. Today* 149 (2010) 248–253, <https://doi.org/10.1016/j.cattod.2009.09.017>.
- [43] Y.J.O. Asencios, E.M. Assaf, Combination of dry reforming and partial oxidation of methane on NiO-MgO-ZrO<sub>2</sub> catalyst: effect of nickel content, *Fuel Process. Technol.* 106 (2013) 247–252, <https://doi.org/10.1016/j.fuproc.2012.08.004>.
- [44] J.G. Seo, M.H. Youn, J.C. Jung, K.M. Cho, S. Park, I.K. Song, Preparation of Ni/Al<sub>2</sub>O<sub>3</sub>-ZrO<sub>2</sub> catalysts and their application to hydrogen production by steam reforming of LNG: effect of ZrO<sub>2</sub> content grafted on Al<sub>2</sub>O<sub>3</sub>, *Catal. Today* 138 (2008) 130–134, <https://doi.org/10.1016/j.cattod.2008.05.006>.
- [45] H. Li, J. Ren, X. Qin, Z. Qin, J. Lin, Z. Li, Ni/SBA-15 catalysts for CO methanation: effects of V, Ce, and Zr promoters, *RSC Adv.* 5 (2015) 96504–96517, <https://doi.org/10.1039/c5ra15990c>.
- [46] G.S. Wu, L.C. Wang, Y.M. Liu, Y. Cao, W.L. Dai, H.Y. He, K.N. Fan, Implication of the role of oxygen anions and oxygen vacancies for methanol decomposition over zirconia supported copper catalysts, *Appl. Surf. Sci.* 253 (2006) 974–982, <https://doi.org/10.1016/j.apsusc.2006.01.056>.
- [47] W. Li, X. Nie, X. Jiang, A. Zhang, F. Ding, M. Liu, Z. Liu, X. Guo, C. Song, ZrO<sub>2</sub> support imparts superior activity and stability of Co catalysts for CO<sub>2</sub> methanation, *Appl. Catal. B Environ.* 220 (2018) 397–408, <https://doi.org/10.1016/j.apcatb.2017.08.048>.
- [48] L. Lin, K. Wang, K. Yang, X. Chen, X. Fu, W. Dai, The visible-light-assisted thermocatalytic methanation of CO<sub>2</sub> over Ru/TiO<sub>2-x</sub>N<sub>x</sub>, *Appl. Catal. B Environ.* 204 (2017) 440–455, <https://doi.org/10.1016/j.apcatb.2016.11.054>.
- [49] D. Chen, D. He, J. Lu, L. Zhong, F. Liu, J. Liu, J. Yu, G. Wan, S. He, Y. Luo, Investigation of the role of surface lattice oxygen and bulk lattice oxygen migration of cerium-based oxygen carriers: XPS and designed H<sub>2</sub>-TPR characterization, *Appl. Catal. B Environ.* 218 (2017) 249–259, <https://doi.org/10.1016/j.apcatb.2017.06.053>.
- [50] K.M. Lee, W.Y. Lee, Partial oxidation of methane to syngas over calcined Ni-Mg/Al layered double hydroxides, *Catal. Lett.* 83 (2002) 65–70, <https://doi.org/10.1023/A:1020609632354>.
- [51] N. Perkas, G. Amirian, Z. Zhong, J. Teo, Y. Gofer, A. Gedanken, Methanation of Carbon Dioxide on Ni catalysts on mesoporous ZrO<sub>2</sub> doped with rare earth oxides, *Catal. Lett.* 130 (2009) 455–462, <https://doi.org/10.1007/s10562-009-9952-8>.
- [52] Y. Wang, J. Ren, Y. Wang, F. Zhang, X. Liu, Y. Guo, G. Lu, Nanocasted synthesis of mesoporous LaCoO<sub>3</sub> perovskite with extremely high surface area and excellent activity in methane combustion, *J. Phys. Chem. C* 112 (2008) 15293–15298, <https://doi.org/10.1021/jp8048394>.
- [53] B. Miao, S.S.K. Ma, X. Wang, H. Su, S.H. Chan, Catalysis mechanisms of CO<sub>2</sub> and CO methanation, *Catal. Sci. Technol.* 6 (2016) 4048–4058, <https://doi.org/10.1039/C6CY00478D>.
- [54] X. Liu, P. Ning, L. Xu, Q. Liu, Z. Song, Q. Zhang, Low-temperature catalytic oxidation of CO over highly active mesoporous Pd/CeO<sub>2</sub>-ZrO<sub>2</sub>-Al<sub>2</sub>O<sub>3</sub> catalyst, *RSC Adv.* 6 (2016) 41181–41188, <https://doi.org/10.1039/C6RA05193F>.
- [55] M.A.A. Aziz, A.A. Jalil, S. Triwahyono, R.R. Mukti, Y.H. Taufiq-Yap, M.R. Sazegar, Highly active Ni-promoted mesostructured silica nanoparticles for CO<sub>2</sub> methanation, *Appl. Catal. B Environ.* 147 (2014) 359–368, <https://doi.org/10.1016/j.apcatb.2013.09.015>.
- [56] M.A.A. Aziz, A.A. Jalil, S. Triwahyono, A. Ahmad, CO<sub>2</sub> methanation over heterogeneous catalysts: recent progress and future prospects, *Green Chem.* 17 (2015) 2647–2663, <https://doi.org/10.1039/C5GC00119F>.